Volume 4
Number 7
July 2025
Pages 1653-1976

Digital Discovery

rsc.li/digitaldiscovery

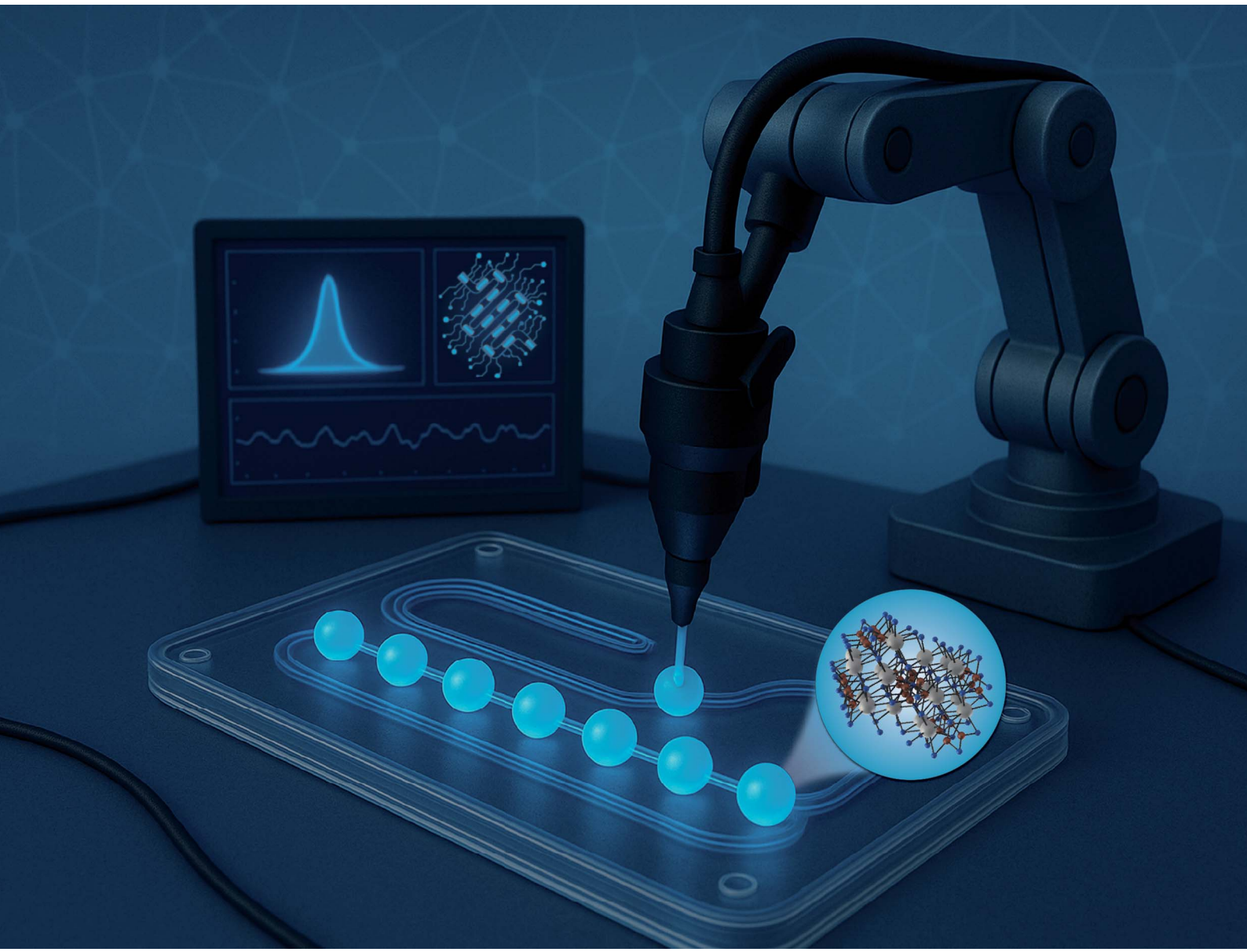

ISSN 2635-098X

ROYAL SOCIETY OF CHEMISTRY

PAPER
Milad Abolhasani *et al.*
A self-driving fluidic lab for data-driven synthesis of lead-free perovskite nanocrystals

Digital Discovery

ROYAL SOCIETY OF CHEMISTRY

PAPER

View Article Online
View Journal | View Issue

Cite this: *Digital Discovery*, 2025, **4**, 1722

A self-driving fluidic lab for data-driven synthesis of lead-free perovskite nanocrystals†

Sina Sadeghi,‡[a] Karl Mattsson,‡[a] Joshua Glasheen,[a] Victoria Lee,[b] Christine Stark,[a] Pragyan Jha,[a] Nikolai Mukhin,[a] Junbin Li,[a] Arup Ghorai,[a] Negin Orouji,[a] Christopher H. J. Moran,[a] Alireza Velayati,[a] Jeffrey A. Bennett,[a] Richard B. Canty,[a] Kristofer G. Reyes[c] and Milad Abolhasani *[a]

Copper (Cu)-based metal halide perovskite (MHP) nanocrystals (NCs) have recently gained attention as promising Pb-free and environmentally sustainable alternatives to traditional Pb-based MHPs, offering wide bandgaps, large Stokes shifts, and high emission stability. Despite these advantages, achieving high photoluminescence quantum yields (PLQYs) in Cu-based MHP NCs remains challenging, which impedes their widespread deployment in advanced optoelectronic and energy-related devices. Introducing a metal halide additive in the precursor chemistry can enhance the optical performance of Cu-based MHP NCs, but this approach substantially expands the experimental parameter space, rendering conventional batch-based, trial-and-error methods both time- and resource-intensive. Here, we present a self-driving fluidic lab (SDFL) that combines a modular microfluidic reactor, real-time *in situ* characterization, and machine-learning-guided decision-making to autonomously explore and optimize high-dimensional Cu-based MHP NC syntheses in the presence of a metal halide additive. Leveraging droplet-based flow chemistry and ensemble neural network-enabled Bayesian optimization, our SDFL rapidly navigates complex precursor formulations and reaction conditions of Cu-based MHP NCs, thus minimizing waste and accelerating discovery. We utilize the SDFL with three distinct precursor chemistries to synthesize $Cs_3Cu_2I_5$ NCs, with zinc iodide (ZnI_2) serving as the metal halide additive. The high-fidelity data generated *in situ* allow for the creation of predictive digital twin models that yield mechanistic insights into additive-assisted NC formation. By iteratively refining synthesis parameters within the SDFL, we achieve $Cs_3Cu_2I_5$ NCs with post-purification PLQYs of approximately 61%, marking a significant improvement over conventional Cu-based MHP NCs. The resulting high-performance, Pb-free NCs underscore the potential of sustainable materials acceleration platforms to speed-up the development of next-generation photonic and energy technologies.

Received 13th February 2025
Accepted 24th April 2025

DOI: 10.1039/d5dd00062a

rsc.li/digitaldiscovery

1 Introduction

Metal halide perovskite (MHP) nanocrystals (NCs) represent a cutting-edge class of colloidal semiconductor nanomaterials renowned for their impressive optoelectronic properties, including high photoluminescence quantum yield (PLQY), narrow emission linewidth, and adjustable optical characteristics through size, composition, and surface chemistry fine-tuning.[1,2] These unique features make MHP NCs highly adaptable for diverse applications in photonic and energy technologies,[3–5] such as light-emitting diodes (LEDs) and luminescent solar concentrators.[6–12] Moreover, the compatibility of MHP NCs with cost-effective solution-phase synthesis and processing further enhances their potential for scalable manufacturing. Despite their promise, the broad adoption of MHP NCs, particularly lead (Pb)-based variants, faces significant hurdles due to the toxicity of Pb and poor stability in ambient conditions. These challenges underscore the urgent need to develop more stable and environmentally friendly alternatives, paving the way for safer and more robust integration of these colloidal semiconductor materials into next-generation technologies.

Building on the limitations of Pb-based MHP NCs, copper (Cu)-based MHP NCs have emerged as promising Pb-free alternatives, offering significant advantages in terms of sustainability.[13–15] Specifically, $Cs_3Cu_2X_5$ (X = Cl, Br, I) NCs stand out due to their large Stokes shifts and unique self-

[a]*Department of Chemical and Biomolecular Engineering, North Carolina State University, Raleigh, NC 27695, USA. E-mail: abolhasani@ncsu.edu*

[b]*Department of Materials Science and Engineering, University of Pennsylvania, Philadelphia, PA 19104, USA*

[c]*Department of Materials Design and Innovation, University at Buffalo, Buffalo, NY 14260, USA*

† Electronic supplementary information (ESI) available. See DOI: https://doi.org/10.1039/d5dd00062a

‡ Authors contributed equally.

trapped exciton (STE) emissions driven by lattice deformations.[16–20] Such Cu-based MHP NCs exhibit exceptional optical properties, such as a wide bandgap and high emission stability, which makes them ideal for various optoelectronic applications, including ultraviolet (UV) photodetectors, X-ray imaging, and anticounterfeiting technologies.[21–25] In addition, Cu-based MHP NCs overcome some key challenges associated with Pb-containing variants: high stability under ambient conditions has been achieved with cesium copper iodide ($Cs_3Cu_2I_5$)—a zero-dimensional MHP with an orthorhombic crystal structure—and the use of Cu, an earth-abundant and minimally toxic element, circumvents the health and safety hazards of Pb.[13] These advantages, combined with their compatibility with scalable, cost-effective manufacturing methods, position Cu-based MHP NCs as a sustainable candidate for next-generation photonic and energy devices.

While significant progress has been achieved in the development and application of Cu-based MHP NCs, challenges persist in achieving high-performing NCs, limiting both their practical device applications and further exploration in fundamental research. Addition of metal halide additives in the halide source precursor has emerged as an effective strategy to enhance the PLQY and morphology uniformity of $Cs_3Cu_2I_5$ NCs. In one example, Lian *et al.* utilized a modified hot-injection (HI) approach, assisted by indium iodide (InI_3) as the halide source additive that enabled the synthesis at a relatively high temperature, to synthesize $Cs_3Cu_2I_5$ NCs with improved PLQY.[26]

The introduction of a metal halide additive into the synthesis process of Cu-based MHP NCs dramatically expands the experimental parameter space. This complexity stems from the wide variety of potential additives, the varying concentrations, and the intricate interactions between the additive and the primary halide source. These additional factors compound the already intricate synthesis dynamics of MHP NCs, as each parameter can have multifaceted and interdependent effects on the resulting NCs' optical properties. The expanded parameter space makes comprehensive exploration and optimization of Cu-based MHP NCs extremely challenging. Conventional batch-based trial-and-error methods, which involve sequentially adjusting one variable at a time, become not only time-consuming and labor-intensive but also highly inefficient, leading to significant material consumption, increased costs, and considerable waste generation. Such methods are fundamentally inadequate to match the rapid pace of development required for advancing Pb-free MHP NC technologies.[27–29] Therefore, there is a critical need for high-throughput materials acceleration platforms that can efficiently navigate and optimize this expanded synthesis space while minimizing resource usage and environmental impact.

Self-driving fluidic labs (SDFLs) represent a sustainable materials acceleration platform for expediting development of colloidal NCs and address the limitations of conventional batch-based methods by leveraging automated, high-throughput (reaction miniaturization), and data-driven approaches.[30–32] Unlike traditional batch reactors, droplet-based microfluidic systems enable continuous synthesis, offering exceptional precision and scalability while reducing the inherent variability of batch processes. Additionally, the modular nature of tube-based microfluidic reactors and their compatibility with real-time *in situ* characterization tools, such as spectroscopy, provide fine control over colloidal NC syntheses, allowing for rapid exploration of complex and high-dimensional experimental parameter spaces.[29,33,34] Additionally, microfluidic NC synthesis produces high-quality data with low experimental noise, a crucial factor for training predictive machine learning (ML) models.[35,36] By integrating microfluidic technology with an ML agent, SDFLs create a fully automated closed-loop workflow for sustainable autonomous experimentation. An SDFL generates hypotheses, plans experiments to be autonomously executed, and automatically analyzes results to refine the process iteratively. ML techniques like Bayesian optimization (BO) enable SDFLs to intelligently navigate vast and interdependent synthesis spaces, identifying optimal conditions while minimizing uncertainties. The miniaturized reaction volumes in microfluidics not only reduce material consumption and costs but also mitigate waste, making the overall materials acceleration platform both more efficient and environmentally sustainable. SDFLs' ability to combine precision synthesis with ML-assisted decision-making ensures faster progress in understanding and tailoring precursor formulation-synthesis-property relationships. SDFLs hold immense potential for advancing nanoscience research, offering a scalable and eco-conscious solution to meet the increasing demands of modern scientific and industrial applications in clean energy and sustainability.

Herein, we present an SDFL for autonomous high-dimensional parameter space exploration of Cu-based MHP NC synthesis with a metal halide additive. The developed SDFL is compatible with three different precursor chemistries associated with Cu-based MHP NCs, incorporating zinc iodide (ZnI_2) as the halide additive. It consists of a modular flow chemistry platform as the primary hardware and an ML agent using ensemble neural network (ENN)-based BO for real-time synthesis modeling and decision-making. Specifically, we utilize the developed SDFL to investigate the role of a halide additive (ZnI_2) in enhancing the optical properties of $Cs_3Cu_2I_5$ NCs and rapidly discover the optimal synthetic route of the highest-performing NCs (*i.e.*, maximum PLQY) through a one-pot heat-up synthesis approach. The resulting high-performing Pb-free MHP NCs demonstrate exceptional potential as key components in printed clean technologies, showcasing the transformative impact of SDFLs in materials science and sustainability in general. Fig. 1 presents an overview of the developed SDFL for autonomous in-flow synthesis and optimal synthetic route discovery of $Cs_3Cu_2I_5$ NCs assisted by the halide additive, ZnI_2.

2 Experimental

2.1 Chemicals

Oleic acid (OA, 90%) and Hexane (70%) were purchased from Sigma-Aldrich. 1-Octadecene (ODE, 90%), *n*-octylamine (OAm, 98%), copper(I) iodide (CuI, 99.995% trace metal basis), zinc iodide (ZnI_2, 99.995% metals basis), and cesium carbonate

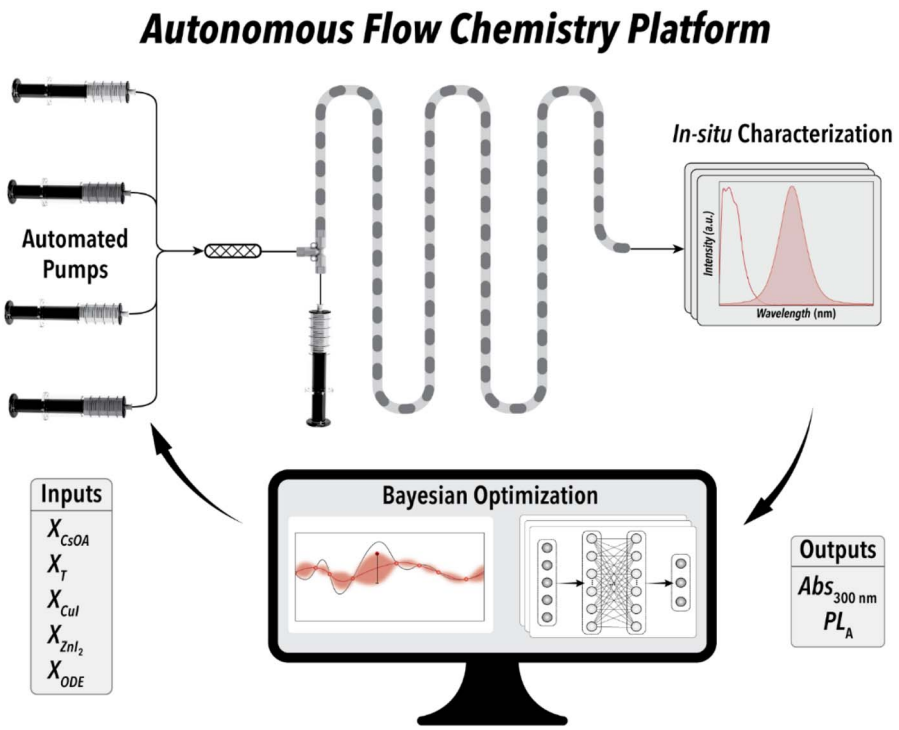

Fig. 1 Illustration of an autonomous fluidic lab for closed-loop synthesis science studies of Cu-based MHP NCs.

(Cs_2CO_3, 99.994% metals basis) were purchased from Fisher Scientific. High-performance heat transfer perfluorinated oil (PFO) was purchased from Solvay. All chemicals were used without further purification.

2.2 Precursor preparation

The precursor chemistry reported by Qu *et al.* was adapted with salt to ligand ratio adjustments to achieve a soluble Cs-oleate (CsOA) precursor at room temperature amenable to the in-flow NC synthesis.[37] As reported in our group's prior work, soluble precursor stock solutions are crucial for reproducible in-flow synthesis of MHP NCs.[35]

Three different precursor chemistries were considered in this study. In precursor chemistry 1 ($Chem_1$), a transparent and room temperature-stable CsOA precursor was prepared by increasing the Cs : OA molar ratio. In precursor chemistry 2 ($Chem_2$), the halide source precursor solutions were also adjusted according to the CsOA precursor modification. Precursor chemistry 3 ($Chem_3$) was similar to $Chem_2$ with a minor difference where the halide source and CsOA precursor concentrations were increased by 11%. All three precursor chemistries were further diluted by ODE (5×, 5×, and 1.5×, respectively) to achieve the initial precursor solutions for the in-flow synthesis science studies of $Cs_3Cu_2I_5$ NCs.

2.2.1 $Chem_1$

2.2.1.1 CuI. 0.48 mmol CuI, 0.48 mL OA, 0.6 mL OAm, and 49.32 mL ODE were loaded into a 100 mL 3-neck flask and maintained under vacuum for 1 h at 120 °C. The solution was subsequently purged with nitrogen (N_2) at 120 °C for 30 min.

2.2.1.2 ZnI_2. 0.36 mmol ZnI_2, 0.48 mL OA, 0.6 mL OAm, and 49.32 mL ODE were loaded into a 100 mL 3-neck flask and maintained under vacuum for 1 h at 120 °C. The solution was subsequently purged with N_2 at 120 °C for 30 min.

2.2.1.3 CsOA. 2.024 mmol Cs_2CO_3, 8.28 mL OA, and 42.32 mL ODE were loaded into a 100 mL 3-neck flask which was then maintained under vacuum for 1 h at 120 °C. The mixture was subsequently heated under N_2 to 150 °C and maintained at this temperature for 30 min to ensure a complete conversion of the Cs salt.

2.2.2 $Chem_2$

2.2.2.1 CuI. 0.48 mmol CuI, 1.44 mL OA, 1.8 mL OAm, and 47.16 mL ODE were loaded into a 100 mL 3-neck flask and maintained under vacuum for 1 h at 120 °C. The solution was subsequently purged with N_2 at 120 °C for 30 min.

2.2.2.2 ZnI_2. 0.36 mmol ZnI_2, 1.44 mL OA, 1.8 mL OAm, and 47.16 mL ODE were loaded into a 100 mL 3-neck flask and maintained under vacuum for 1 h at 120 °C. The solution was subsequently purged with N_2 at 120 °C for 30 min.

2.2.2.3 CsOA. 2.024 mmol Cs_2CO_3, 8.28 mL OA, and 42.32 mL ODE were loaded into a 100 mL 3-neck flask which was then maintained under vacuum for 1 h at 120 °C. The mixture was subsequently heated under N_2 to 150 °C and maintained at this temperature for 30 min to ensure a complete conversion of the Cs salt.

2.2.3 $Chem_3$

2.2.3.1 CuI. 0.533 mmol CuI, 1.6 mL OA, 2 mL OAm, and 46.8 mL ODE were loaded into a 100 mL 3-neck flask and maintained under vacuum for 1 h at 120 °C. The solution was subsequently purged with N_2 at 120 °C for 30 min.

2.2.3.2 ZnI_2. 0.4 mmol ZnI_2, 1.6 mL OA, 2 mL OAm, and 46.8 mL ODE were loaded into a 100 mL 3-neck flask and maintained under vacuum for 1 h at 120 °C. The solution was subsequently purged with N_2 at 120 °C for 30 min.

2.2.3.3 CsOA. 2.249 mmol Cs_2CO_3, 9.2 mL OA, and 41.4 mL ODE were loaded into a 100 mL 3-neck flask which was then maintained under vacuum for 1 h at 120 °C. The mixture was subsequently heated under N_2 to 150 °C and maintained at this temperature for 30 min to ensure a complete conversion of the Cs salt.

All precursor stock solutions were given time to cool down and reach room temperature before loading into the gas-tight syringes under inert conditions.

3 Results and discussion

Building a robust SDFL involves seamlessly integrating both physical and digital components to create a highly efficient and autonomous system. On the physical side, advanced microscale fluidic platforms and multimodal *in situ* diagnostics form the foundation for executing experiments with minimal human intervention. On the digital front, ML models, data acquisition pipelines, and real-time optimization algorithms process and analyze experimental data, enabling dynamic decision-making. Automation of the experiment-selection process *via* a data-driven ML agent not only accelerates nanomaterial synthetic route discovery process but also enables researchers to uncover novel relationships within the chemical space that traditional methods might overlook. Reliable automation is crucial in this context, as it ensures consistency and accuracy in executing experimental protocols, providing high-quality data (reproducible with minimal variance) for ML agents of the SDFL. This reliability is essential for training predictive NC synthesis models, allowing them to uncover complex relationships within the experimental space and make accurate predictions. Reducing the automated material synthesis error will significantly reduce the time and resources required for autonomous material synthesis optimization, thereby lowering overall experimental costs and enhancing efficiency in material discovery workflows. Together, the synergy between physical precision and digital intelligence enables SDFLs to accelerate discovery and development of advanced functional materials.

Exploring the complex synthesis space of Pb-free MHP NCs brings a formidable challenge due to the intricate interplay of variables required to achieve superior optical properties. Conventional high-throughput screening methods, while effective for limited parameter spaces, are resource-intensive, time-consuming, and often constrained to local optima, relying heavily on manual oversight and expert guidance. In our recent work, we studied the HI synthesis of $Cs_3Cu_2I_5$ NCs and reported a post-purification PLQY of ~% 17 for the best-performing NC.[35] Building off of the developed digital and physical infrastructure in our prior work, in this study, we build and deploy an SDFL to autonomously investigate a one-pot heat-up synthesis of Pb-free MHP NCs in the presence of a metal halide additive (ZnI_2) to significantly boost the optical properties of $Cs_3Cu_2I_5$ NCs. We primarily focus on synthesizing $Cs_3Cu_2I_5$ NCs with PLQYs higher than the ones synthesized without a metal halide additive.

The developed SDFL in this work utilizes a data-driven ML agent to rapidly explore the large, multivariable synthesis space of Pb-free MHP NCs in the presence of ZnI_2. By eliminating the need for exhaustive trial-and-error experiments, the developed SDFL minimizes resource expenditure and rapidly converges on the optimal synthetic route of the highest-performing Pb-free MHP NCs. The ability to dynamically adapt experimental parameters in response to real-time feedback from an automated material synthesis platform ensures precise, efficient exploration, paving the way to produce high-performing Pb-free MHP NCs in a fraction of the time previously required.

In the next subsections, we discuss the SDFL hardware and its robustness in generating high-quality NC synthesis data. Next, we present the use of the in-house-generated experimental data to train predictive ML models (*i.e.*, digital twins) tailored to the NC precursor chemistries of interest, providing valuable insights into the reaction mechanisms underlying the in-flow synthesis of $Cs_3Cu_2I_5$ NCs. The digital twin term used in this work refers to a robust surrogate model with fairly accurate prediction accuracy which provides mechanistic insight into the reaction mechanism and also guides iterative improvements in optimization campaigns. Leveraging the trained digital twins as surrogate models, we utilize the SDFL to conduct autonomous optimization campaigns to rapidly discover the optimal synthetic route of high-performing $Cs_3Cu_2I_5$ NCs with significantly enhanced PLQYs.

3.1 SDFL hardware

The SDFL hardware, illustrated in Fig. 2 and S1 (ESI),† was specifically designed for rapid and continuous experimentation as well as autonomous manufacturing of Cu-based MHP NCs *via* a one-pot heat-up synthesis approach. Four modules, including fluid delivery, precursor mixing, synthesis, and *in situ* characterization, were incorporated into the SDFL hardware. Five syringe pumps (Chemyx Fusion 6000) were equipped with gas-tight stainless-steel syringes (Chemyx) for accurate, continuous, and automated precursor delivery utilizing a desired volumetric flowrate. Fluorinated ethylene propylene (FEP) tubing (1/16″ outer diameter, OD × 0.02″ inner diameter, ID) was utilized to connect all precursor streams to the fluidic manifolds. Three 50 mL and one 100 mL syringes were utilized to deliver CuI, ZnI_2, CsOA, and ODE to a five-way manifold (IDEX) where the precursor mixture is formed. The precursor mixture (*i.e.*, the reactive phase) was then guided to a T-junction (IDEX) using an in-line static micro-mixer to be combined with an inert carrier fluid, PFO.[38] The inert carrier phase was continuously delivered to the segmentation module using a stainless-steel syringe (100 mL gas-tight syringe, Chemyx), to form a two-phase liquid–liquid segmented flow. The segmented flow was then passed through a custom-built flow reactor module utilizing perfluroalkoxy (PFA) tubing (1/16″ OD × 0.03″ ID) placed inside a custom-designed and CNC-machined aluminum plate for rapid and on-demand heating. Three cartridge heaters (Watlow) and a PID temperature controller

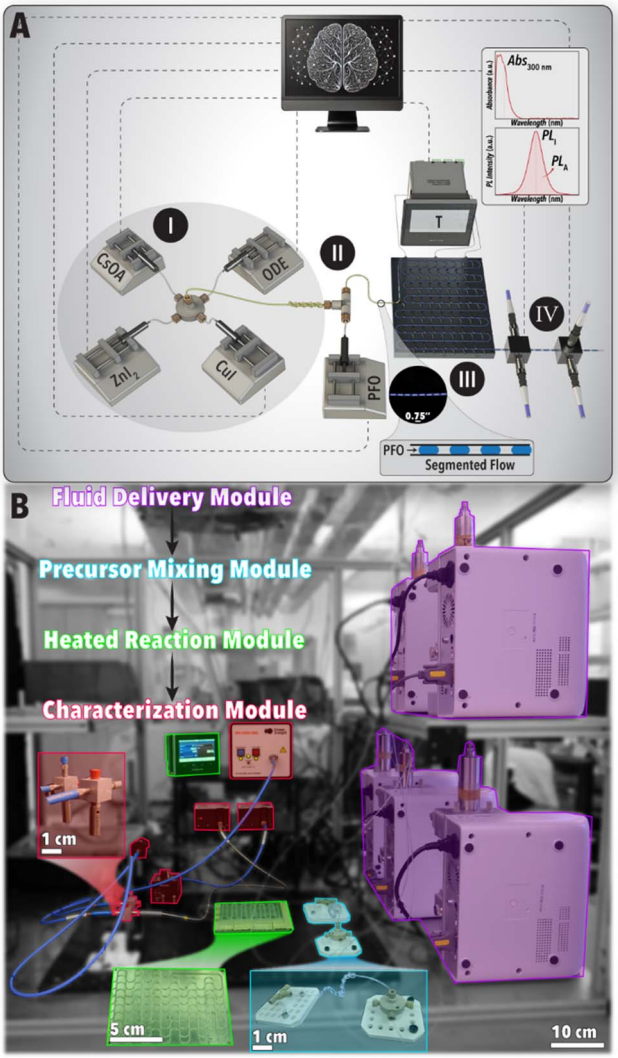

Fig. 2 The developed SDFL for autonomous manufacturing and optimal synthetic route discovery of $Cs_3Cu_2I_5$ NCs utilizing a one-pot heat-up synthesis approach in the presence of a halide additive, ZnI_2: (A) schematic illustration of the (I) fluid delivery, (II) precursor mixing, (III) flow reactor, and (IV) *in situ* characterization modules of the SDFL. (B) A color-coded image of the SDFL.

(F4T, Watlow) were utilized to control the reaction temperature in the heating plate, ranging from 120 °C to 180 °C. The total volumetric flowrate of both reactive and the carrier phase was utilized to control the reaction time in the flow reactor, varying from 40 s to 60 s. The reactive phase was subsequently cooled to room temperature and entered the characterization module using FEP tubing (1/16″ OD × 0.04″ ID). The optical properties of the in-flow synthesized $Cs_3Cu_2I_5$ NCs were then automatically acquired using two bespoke flowcells equipped with two fiber-coupled spectrometers for UV-Vis absorption and photoluminescence (PL) spectroscopy. Five independent input parameters, including the volumetric flowrates of CuI, ZnI_2, CsOA, and ODE streams as well as the reaction temperature were considered to control the automated in-flow synthesis of Pb-free MHP NCs. To ensure reliable and prolonged operation of the segmented flow reaction within the SDFL hardware, the PFO volumetric flowrate was automatically adjusted to half of the precursor mixture's total volumetric flowrate at each reaction condition selected by the ML agent of the developed SDFL. It is worth mentioning that the developed SDFL could explore up to 90 different NC synthesis conditions using a single batch of initial precursor solutions without the need for precursor refilling.

Both the throughput and speed of the SDFL's *in situ* characterization technique are crucial to achieve reliable autonomous experimentation. Fig. S2 (ESI†)† presents benchmarking results of the SDFL's *in situ* characterization (UV-Vis absorption and PL spectroscopy) *vs.* an *ex situ* benchtop spectrometer (FS5 spectrofluorometer, Edinburgh Instruments) using the same as-synthesized NCs. The *in situ* acquired UV-Vis absorption and PL spectra were then utilized to obtain an *in situ* relative PLQY proxy as the key NC property of interest for the subsequent autonomous experimentation campaigns. The *in situ* PLQY proxy was then validated against *ex situ* PLQY measurements (FS5 spectrofluorometer, Edinburgh Instruments) for the same in-flow synthesized NCs. Fig. S3A and S3B (ESI)† show the linear correlation of the *in situ* PLQY proxy *vs.* the *ex situ* measured absolute PLQY for the as-synthesized and purified samples, respectively. Detailed information regarding the calculation of *in situ* PLQY proxy can be found in the ESI (see S3).†

3.1.1 SDFL automation. Achieving fully autonomous experimentation requires a robust process automation strategy that seamlessly coordinates experiment execution with data collection and analysis. In this work, we developed a custom process automation workflow (LabView) to orchestrate the operation of the SDFL hardware (modular flow chemistry platform). We also implemented a data processing strategy (Python) to analyze the optical properties of the Pb-free MHP NCs automatically synthesized by the SDFL. The process automation workflow (LabView) governs the fluid delivery system with five syringe pumps, ensuring NC precursor solutions are directed to the mixing and segmentation modules of the SDFL only after the system stabilizes at the desired reaction temperature. This automation framework also facilitates the automated collection of UV-Vis absorption and PL spectra once the equilibrium waiting time (t_E) has been reached, ensuring data acquisition occurs under steady-state synthesis conditions. Detailed information of the developed process automation module can be found in the ESI (see S4).†

3.1.2 SDFL reliability. SDFL's reliable and prolonged operation as well as reproducible NC synthesis are crucial for accelerated exploration of high-dimensional reaction spaces. To this end, we assessed the robustness of the developed SDFL hardware for the automated continuous flow synthesis of $Cs_3Cu_2I_5$ NCs. Three *in situ*-obtained optical features, including absorbance at 300 nm ($Abs_{300\ nm}$), emission peak intensity (PL_I), and emission peak area (PL_A), were monitored to examine the reliability of the developed SDFL for the continuous flow synthesis of Pb-free MHP NCs. Fig. 3A presents the results of the hardware reliability test throughout a continuous flow NC synthesis for 30 min. The steady-state operation was achieved in two times the residence time ($t_E = 2\times\tau$) with the standard

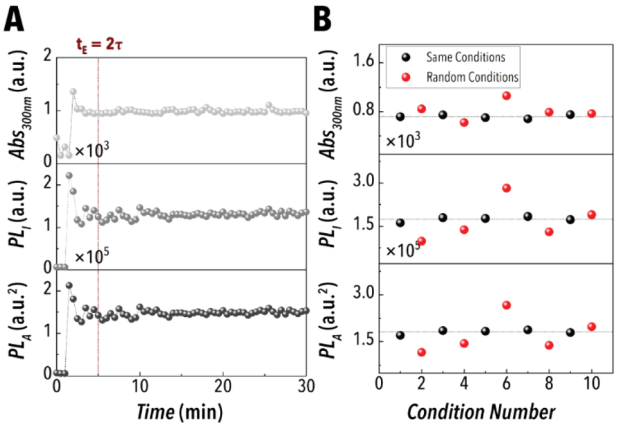

Fig. 3 Evaluation of the SDFL's hardware robustness for prolonged operation and reproducible in-flow synthesis of Cu-based MHP NCs: (A) time-resolved progression of $Abs_{300\ nm}$, PL_I, and PL_A under a specific synthesis condition over 30 min. (B) Reproducibility studies of the SDFL hardware through a cross-contamination study.

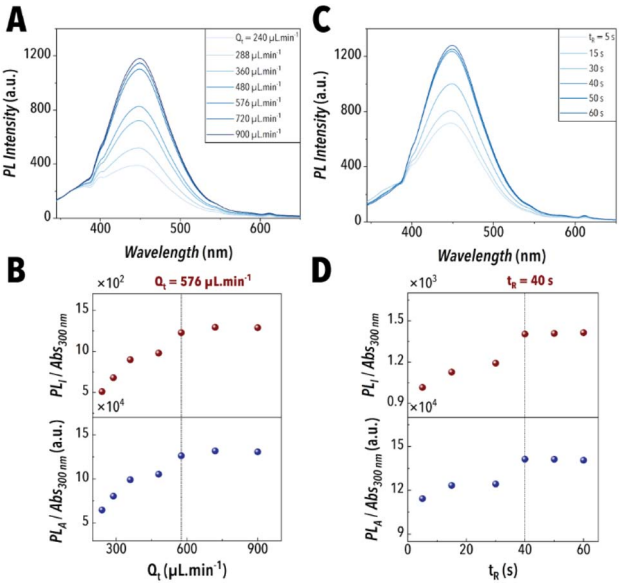

Fig. 4 In-flow studies of the effect of total volumetric flowrate on (A) the PL spectra and (B) the emission optical features (PL_I and PL_A) normalized by $Abs_{300\ nm}$ at a constant residence (reaction) time. The effect of reaction time on (C) the PL spectra and (D) the emission optical features (PL_I and PL_A) normalized by $Abs_{300\ nm}$ at a constant total volumetric flowrate of 720 µL min^{-1} to ensure the NC synthesis reaction is not mass transfer limited.

deviations of 3.1%, 5.2%, and 4.2% for $Abs_{300\ nm}$, PL_I, and PL_A, respectively after reaching steady-state operation. Here, τ refers to the duration required for the fluid to travel from the segmentation manifold to the *in situ* characterization module. Next, we conducted a cross-contamination test between different NC synthesis conditions using a series of random sampling and a constant baseline condition. Briefly, a predetermined synthesis condition was considered as a reference, and a randomly chosen experimental condition was introduced once the SDFL hardware reached steady-state operation for the reference condition. After five reference repetitions, as depicted in Fig. 3B, the cross-contamination analysis revealed the standard deviations of 3.7%, 4.2%, and 3.4% for $Abs_{300\ nm}$, PL_I, and PL_A, respectively. The results presented in Fig. 3 demonstrate the robustness and reliability of the SDFL hardware (shown in Fig. 2), for automated/autonomous synthesis of Pb-free MHP NCs with minimal variance.

Enhanced and uniform mixing of the reactive phase droplets as they move along the flow synthesis module of the SDFL are important for reliable automated synthesis of colloidal NCs. Mixing efficiency of the multi-phase flow format utilized in the developed SDFL is governed by the average flow velocity, which is controlled by the total volumetric flowrate. Thus, in the next step, we examined how varying the total volumetric flowrate affects the in-flow synthesis of $Cs_3Cu_2I_5$ NCs in the presence of a metal halide additive. The microreactor volume (*i.e.*, the length of the tubular flow reactor) placed in the heating plate was adjusted to accommodate a constant reaction time for different total volumetric flowrates. As shown in Fig. 4A, B, and S5A (ESI),† the in-flow NC synthesis was limited by insufficient mass transfer at relatively low total volumetric flowrates, leading to suboptimal mixing. However, when the total volumetric flowrate exceeded 576 µL min^{-1}, the PL spectra of the in-flow synthesized NCs reached a plateau, indicating the reaction is no longer operating within the mass transfer-limited regime. The results shown in Fig. 4 further highlight the importance of conducting reproducibility and reliability studies of SDFL hardware through precursor mixing tests. Next, we investigated the role of reaction time on the synthesis of colloidal $Cs_3Cu_2I_5$ NCs within the reaction-limited regime. For this test, a constant total volumetric flowrate of 720 µL min^{-1} with different flow reactor volumes were utilized to accommodate reaction times ranging from 5 s to 60 s. As shown in Fig. 4C, D, and S5B (ESI),† the optical properties of the in-flow synthesized $Cs_3Cu_2I_5$ NCs reached a plateau at reaction times exceeding 40 s. Thus, we utilized total volumetric flowrates ranging from 600 µL min^{-1} to 900 µL min^{-1} and reaction times varying from 40 s to 60 s for subsequent autonomous experimentation campaigns to ensure that the reaction is not mass transfer-limited and also the formation of colloidal NCs is completed within the SDFL's flow reactor module.

3.2 ML agent

The SDFL's ML agent plays a pivotal role in optimizing the NC synthesis process, enabling intelligent decision-making through predictive modeling and adaptive learning using the experimental data generated by the SDFL hardware. Achieving such datasets requires an unbiased sampling approach to comprehensively capture the full spectrum of the NC synthesis parameter space, minimizing the risk of overfitting or bias in the ML model. To address the potential bias issue, we employed the Latin Hypercube Sampling (LHS) strategy, that is a well-established sampling technique for generating well-distributed, high-quality data across the NC synthesis space. LHS partitions the ranges of each input parameter, then ensures every partition is sampled exactly once. This approach

thus allows a systematic exploration of the synthesis conditions while avoiding redundancy and ensuring comprehensive coverage of the parameter space, which provides a broadly dispersed and diverse dataset enhancing the ML model accuracy and the synthesis space exploration efficiency. The experimental data generated by the SDFL's automation mode using the LHS strategy can then be utilized for two purposes. First, training an accurate predictive ML model that acts as the digital twin of the Pb-free MHP NC synthesis process enables rapid simulations and deeper insights into the underlying NC synthesis mechanisms. Second, training a BO algorithm's surrogate ML model for autonomous synthetic route discovery of high-performing Cu-based MHP NC leverages the synergy between data-driven learning and experimental automation to ensure both efficiency and precision in the development of Pb-free MHP NCs.

Herein, we first focused on establishing a global learning framework, where 60 LHS-selected NC synthesis experiments were automatically carried out for each Pb-free MHP precursor chemistry, providing an unbiased dataset. The SDFL-generated dataset was subsequently utilized to construct an ML predictive model for the metal halide additive-assisted Pb-free MHP NC synthesis. An ENN was employed to train the digital twin for each precursor chemistry, mapping five independent input parameters, including the reaction temperature and the volumetric flowrates of CuI, ZnI_2, CsOA, and ODE streams, to two output parameters, $Abs_{300\ nm}$ and PL_A. The aforementioned optical features were then utilized to obtain the PLQY proxy considered as the key objective function to be maximized in autonomous campaigns. The digital twins of different precursor chemistries trained with the LHS datasets were then utilized for synthesis science studies of $Cs_3Cu_2I_5$ NCs in the presence of a halide additive. Fig. 5A–I illustrate the prediction accuracy of the digital twins trained for all three precursor chemistries for both the training and the test datasets. Table S1 (ESI)† represents the LHS experimental conditions with their associated *in situ* measured PLQY proxy for three different precursor chemistries tested in this study ($Chem_1$, $Chem_2$, and $Chem_3$). $Chem_1$ was adapted from a previously reported precursor chemistry in the literature.[37] The Cs : OA molar ratio was adjusted to obtain

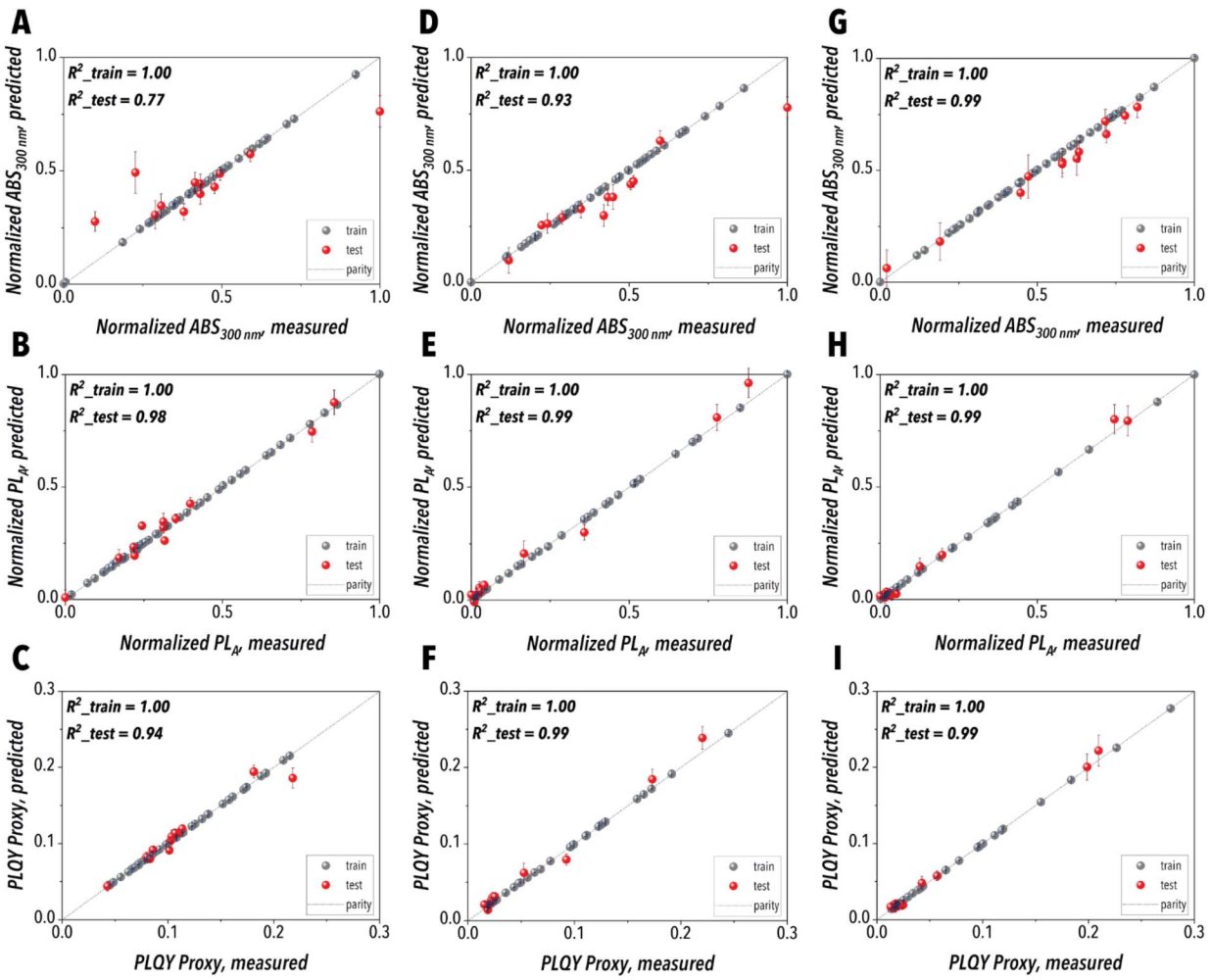

Fig. 5 Digital twin performance evaluation plots for (A, D and G) $Abs_{300\ nm}$, (B, E and H) PL_A, and (C, F and I) PLQY proxy where the left, middle, and right columns are associated with $Chem_1$, $Chem_2$, and $Chem_3$, respectively. The complete lists of the LHS experiments conducted for the precursor chemistries of interest and their corresponding *in situ* measured PLQY proxy are provided in Table S1 (ESI).†

a soluble CsOA precursor solution under ambient conditions, a critical factor for achieving reproducible flow synthesis of colloidal NCs. To prevent excess ligands in the reactive phase, the halide source precursor was not changed from the original precursor chemistry. In $Chem_2$, the ligand concentration in the halide source was accordingly adjusted to match the modified Cs : OA molar ratio, allowing to explore how excess ligands influence the $Cs_3Cu_2I_5$ NCs' PLQY. $Chem_3$ was a more concentrated version of $Chem_2$, designed to examine the effect of initial precursor concentration on the quality of the in-flow synthesized $Cs_3Cu_2I_5$ NCs (*i.e.*, PLQY).

3.3 Data-driven synthesis science studies of $Cs_3Cu_2I_5$ NCs

Next, we conducted Shapley additive explanation (SHAP) analysis on the trained digital twins of all three tested precursor chemistries, which evaluated the contribution of each synthesis input parameter on the optical properties of the in-flow synthesized Pb-free MHP NCs. SHAP analysis results ranked the digital twin model features (independent input variables) based on their influence on the PLQY proxy of Pb-free MHP NCs, offering insights into the relative significance of each NC synthesis parameter for each tested precursor chemistry. Fig. 6A presents the SHAP analysis results attained from the digital twin trained on $Chem_3$ LHS dataset. The SHAP analysis results revealed that CsOA concentration, reaction temperature, and CuI concentration were the most important reaction parameters controlling the synthesis of Pb-free MHP NCs. Based upon the $Chem_3$ SHAP analysis results, the PLQY proxy of $Cs_3Cu_2I_5$ NCs is enhanced as the CsOA precursor concentration decreases in the reactive phase. This finding aligns with prior studies of the Pb-based MHP NCs where the excessive amount of CsOA was reported to initiate side reactions, resulting in NCs with lower PLQY values.[39,40] Additionally, the $Chem_3$ digital twin model revealed that elevating the reaction temperature and CuI precursor concentration boosts the Pb-free MHP NCs' PLQY proxy. The resulting NCs' surface defects as well as non-radiative recombination are elevated as the reaction temperature decreases, which leads to a lower quality NCs (*i.e.*, lower PLQY proxy values).[35,41] Furthermore, increasing the CuI precursor concentration generates a reaction environment abundant in Cu-oleate (CuOA), which facilitates promoting the formation of $Cs_3Cu_2I_5$ NCs, ultimately enhancing the quality of the resulting NCs.[42] Increasing the ZnI_2 precursor concentration was also revealed to enhance the quality of Pb-free MHP NCs. As the concentration of the metal halide additive precursor (ZnI_2) increases, the additional halide ions can passivate the halogen vacancy defects on the surface of the NCs, reducing the non-radiative recombination that ultimately elevates $Cs_3Cu_2I_5$ NCs' PLQY.[37] Additionally, the SHAP results of $Chem_3$ suggested that the ODE stream did not have a significant impact on the optical properties of Pb-free MHP NCs, which can be attributed to the relatively low concentration of the starting NC precursors.

Next, the $Chem_3$ digital twin was utilized to visualize the high-dimensional chemical space of Pb-free MHP NCs. To evaluate how the most important synthesis parameters influence the NCs' PLQY, the three most effective model features, identified by the SHAP analysis, were selected for the surface visualizations. Fig. 6B–D illustrate surface plots that depict the combined impact of each two input parameter pairs (out of the top three-ranked features selected from the SHAP analysis) while the rest of the synthesis parameters remained constant at three levels (low, medium, and high). The results illustrated in the surface plots generated by the $Chem_3$ digital twin further confirm the SHAP analysis results. As illustrated in Fig. 6B, decreasing the CsOA and increasing the CuI precursor concentrations enhance the NCs' PLQY, particularly when a higher reaction temperature and a more concentrated ZnI_2 precursor are utilized. Fig. 6C verifies the direct and reverse correlations of the NCs' PLQY with the reaction temperature and the CsOA precursor concentration, respectively. Furthermore, it is evident that the quality of Pb-free MHP NCs is enhanced as the CuI and ZnI_2 precursor concentrations increase. As presented in Fig. 6D, utilizing a higher reaction temperature and a more concentrated CuI improves the quality of the resulting Pb-free MHP NCs. However, increasing the ZnI_2 precursor concentration could not overcome the detrimental effects that utilizing a more concentrated CsOA precursor would have on the resulting NCs' PLQY. The SHAP analysis results as well as the surface plots obtained from the digital twins trained on $Chem_1$ and $Chem_2$ LHS datasets are presented in Fig. S6 and S7† (ESI†), respectively. The similarity of $Chem_2$ and $Chem_3$ SHAP results is attributed to the fact that the only difference between $Chem_2$ and $Chem_3$ is the initial concentrations of the stock solutions. For $Chem_1$, although CsOA concentration, reaction temperature, and CuI concentration were still ranked as the most effective synthesis parameters, the ZnI_2 precursor concentration was revealed to not affect the $Cs_3Cu_2I_5$ NCs' PLQY much, suggesting that the initial concentration of the ZnI_2 precursor solutions associated with $Chem_1$ was relatively high.

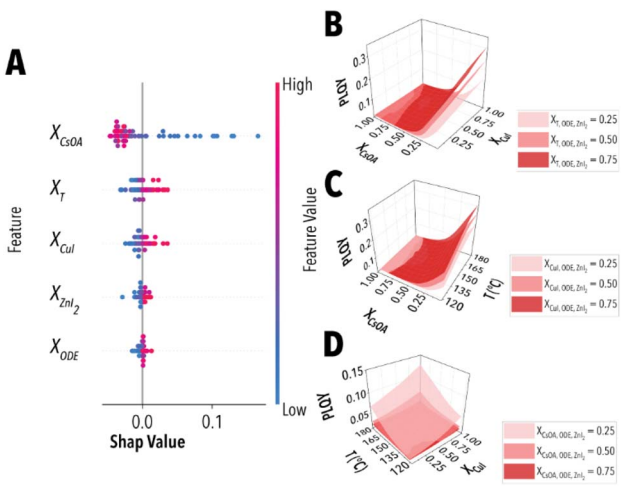

Fig. 6 Data-driven synthesis science studies of ZnI_2-assisted $Cs_3Cu_2I_5$ NC formation using the digital twin model obtained for $Chem_3$: (A) SHAP plot of PLQY proxy; X_T, X_{CsOA}, X_{CuI}, X_{ZnI_2}, and X_{ODE} represent dimensionless independent input parameters associated with reaction temperature and volumetric flowrates of CsOA, CuI, ZnI_2, and ODE streams, respectively. (B–D) Surface plots illustrating the role of the top three most effective synthesis input parameters on PLQY proxy of Pb-free MHP NCs.

Following the digital twin studies of Pb-free MHP NCs, the trained ML model of each precursor chemistry was utilized as a surrogate model for autonomous optimization of $Cs_3Cu_2I_5$ NCs in the presence of ZnI_2. The SDFL's autonomous synthesis optimization of Pb-free MHP NCs included automatic execution of the following five steps iteratively: (i) initializing a predictive surrogate model, (ii) determining the next NC synthesis experimental condition based on a predefined experiment-selection strategy, (iii) automatically conducting the selected NC synthesis experiment using the SDFL hardware, (iv) capturing and analyzing the synthesized NC property in real time, and (v) refining the surrogate model using the expanded experimental dataset. The primary aim of the autonomous campaigns was to leverage prior insights derived from the LHS experiments to efficiently navigate and discover the optimal synthetic route of $Cs_3Cu_2I_5$ NCs, achieving maximum PLQY with minimal experimental iteration/costs. To achieve this goal, an autonomous optimization campaign, constrained to 16 experimental iterations, was carried out for each precursor chemistry using the SDFL. Expected improvement (EI) decision-making policy was utilized for the first 15 iterations followed by pure exploitation (EPLT) employed for the last (16th) iteration. In BO, the EI acquisition function prioritizes sampling points that are likely to outperform the current best observed objective value, balancing exploitation of known high-value regions with exploration in areas of high uncertainty, whereas the EPLT policy focuses solely on refining the highest-performing candidate identified within the explored search space. Fig. 7A presents the results of the autonomous synthesis of Pb-free MHP NCs for three different precursor chemistries. The EI decision policy reached the *in situ* PLQY proxy of 26.7%, 26.9%, and 31.5% for $Chem_1$, $Chem_2$, and $Chem_3$, respectively. It is worth noting that the highest PLQY proxy achieved in each chemistry optimization campaign surpassed the maximum PLQY proxy obtained from the corresponding LHS experiments, which underscores the importance of further strategic exploration within the high-dimensional chemical space to uncover the synthetic pathway for the highest-performing $Cs_3Cu_2I_5$ NCs. The autonomous optimization campaigns were benchmarked against a random sampling campaign executed with the same experimental budget for $Chem_3$. The random sampling approach performed considerably worse, resulting in a maximum *in situ* PLQY proxy of 17.4%. Focusing on maximizing the expected progress, the EI policy accelerates convergence toward optimal conditions more efficiently than the other decision-making strategies.[35,36] The highest-performing $Cs_3Cu_2I_5$ NCs synthesized by the SDFL resulted in post-purification absolute PLQY values of ~49%, ~54%, and ~61% for $Chem_1$, $Chem_2$, and $Chem_3$, respectively, which improves the highest PLQY of $Cs_3Cu_2I_5$ NCs without the halide additive by more than 2.5×. The champion $Cs_3Cu_2I_5$ NCs synthesized in flow with the halide additive exhibit a more than 2.5-fold enhancement in PLQY compared to previously reported flow-synthesized $Cs_3Cu_2I_5$ NCs under additive-free conditions, representing the highest PLQY achieved to date for flow-synthesized Pb-free metal halide perovskite NCs. However, the PLQY of the champion $Cs_3Cu_2I_5$ NCs synthesized in flow with the halide additive remains slightly lower than that of $Cs_3Cu_2I_5$ NCs synthesized in batch reactors under similar halide-assisted conditions, likely due to differences in the solubility and speciation of the initial precursors, which can influence nucleation and growth dynamics in the two reactors.[26,37,42] Progression of the normalized NC synthesis parameters selected by the ML agent throughput the autonomous synthesis campaigns of all three precursor chemistries and the random sampling experiments are shown in Fig. 7B.

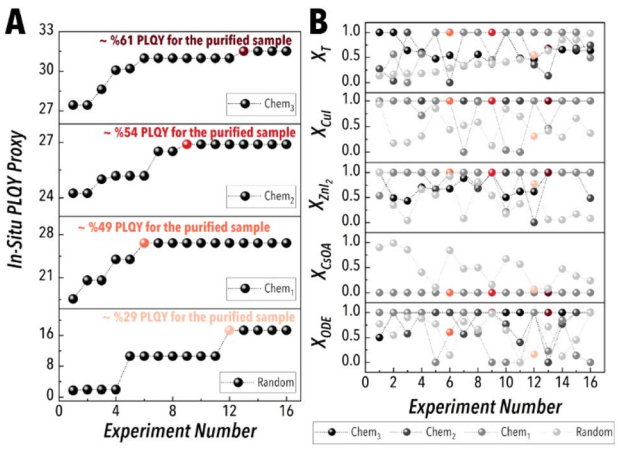

Fig. 7 Results of the autonomous optimization campaigns synthesizing $Cs_3Cu_2I_5$ NCs in the presence of a metal halide additive, ZnI_2. (A) Representation of the best-result-so-far and (B) ML-agent synthesis parameter selection evolution during the autonomous synthesis campaigns of $Cs_3Cu_2I_5$ NCs for different precursor chemistries of interest, benchmarked against a random sampling campaign conducted for $Chem_3$. A complete list of the results of the autonomous and random sampling experiments is provided in Table S2 (ESI).†

Fig. 8 presents optical and structural analysis of the highest-performing $Cs_3Cu_2I_5$ NCs discovered by the SDFL. Fig. 8A illustrates the *in situ* UV-Vis absorption and PL spectra of the highest-performing $Cs_3Cu_2I_5$ NCs, autonomously synthesized by the SDFL using $Chem_3$. Fig. 8B presents the X-ray diffraction (XRD) analysis of the purified high-performing $Cs_3Cu_2I_5$ NCs, illustrating an orthorhombic crystal structure. Major diffraction peaks are indexed, and additional reflections, detected due to the long scan time and fine step size, are consistent with the reference pattern (JCPDS #45-0077).[43] The relatively low intensity is attributed to the thin film used for the XRD analysis,[44,45] while minor extra peaks may arise from unoptimized purification of the autonomously synthesized NCs. Fig. 8C–H display a transmission electronic microscopy (TEM) image and elemental analysis of the champion $Cs_3Cu_2I_5$ NCs, respectively. Fig. 8C illustrates a brick-like shape for $Cs_3Cu_2I_5$ NCs. The lack of Zn in the elemental mapping results indicates that the ZnI_2 precursor did not act as a source of the metal cation dopant and instead served as a metal halide additive, facilitating the formation of Pb-free MHP NCs synthesis at high reaction temperatures.[26] To further confirm the role of ZnI_2, we conducted X-ray photoelectron spectroscopy (XPS) and inductively coupled plasma-optical emission spectrometry (ICP-OES) analyses on the champion $Cs_3Cu_2I_5$ NCs. The XPS results, shown in

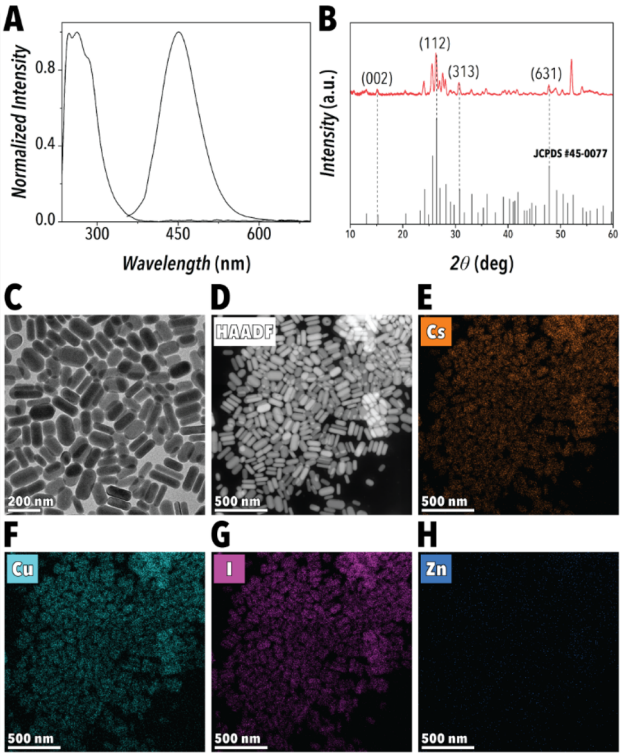

Fig. 8 (A) The in-situ obtained UV-Vis absorption and PL spectra, (B) XRD pattern, (C) TEM image, and (D–H) HAADF-STEM image of the highest-performing $Cs_3Cu_2I_5$ NCs synthesized by the SDFL using the EI decision-making policy.

Fig. S8,† verified that the Zn^{2+} cations were neither doped and nor incorporated within the $Cs_3Cu_2I_5$ host NCs discovered by the SDFL. The amount of Zn detected by the ICP-OES analysis was less than 1% of that of the Cu content (ESI, Table S3†), which could be attributed to a small amount of unreacted ZnI_2 precursor.

4 Conclusions

In conclusion, we demonstrated an SDFL for data-driven synthesis and optimization of Cu-based MHP NCs using a one-pot heat-up approach and a ZnI_2 metal halide additive. The modular flow chemistry platform at the core of the SDFL accommodated three distinct precursor formulations, enabling a reproducible, continuous synthesis of $Cs_3Cu_2I_5$ NCs with markedly enhanced optical properties. By coupling LHS with ENN-driven BO, the SDFL generated high-fidelity experimental data to build a robust digital twin, which not only provided mechanistic insight into the additive-assisted reaction pathways but also guided iterative improvements in PLQY of the Cu-based MHP NCs. This closed-loop, data-driven approach led to the synthetic route discovery of high-performing $Cs_3Cu_2I_5$ NCs with post-purification PLQYs of ~61%, surpassing earlier benchmarks by more than 2.5-fold. The modularity of the SDFL's hardware enables autonomous exploration of other halide additives with precursor chemistries amenable to in-flow synthesis.

The developed SDFL enabled the optimal synthetic route discovery of the highest-performing $Cs_3Cu_2I_5$ NCs within 76 flow experiments while using only a total of 2 mL NC precursors per experimental condition as opposed to 10–100 mL precursors utilized per conventional flask-based batch experiments.[37] The minimal resource consumption and rapid convergence to optimal synthesis conditions highlight the potential of SDFLs to transform materials discovery and manufacturing, particularly for next-generation Pb-free MHP NCs. Our findings underscore the advantage of integrating automated fluidic reactors with real-time characterization and machine learning, enabling a scalable, sustainable route to high-performance nanomaterials. Beyond demonstrating the feasibility of Cu-based MHP NCs as an eco-friendly alternative to Pb-based analogues, this work illustrates the broader promise of autonomous, data-driven platforms to expedite innovation in photonic and energy applications. By reducing both experimentation time and waste, the developed SDFL paves the way for more responsible and efficient development of advanced functional materials.

Code availability

The source codes for data processing and BO algorithm can be accessed *via* our group's GitHub page: **https://github.com/AbolhasaniLab/SDFL-2025** as well as the following DOI: **https://doi.org/10.5281/zenodo.15283084**.

Data availability

The data supporting the findings of this study is available within the main text and the ESI as well as the following DOI: **https://doi.org/10.5281/zenodo.15283084**.

Author contributions

S. S. and K. M. contributed equally to this work. M. A. and S. S. conceived the project. S. S., K. M., J. A. B., N. O., V. L., R. B. C., K. G. R., and M. A. designed the algorithms. S. S. and K. M. programmed the digital twin and Bayesian optimization algorithms and analyzed all experimental data. S. S. designed and built the flow chemistry platform with J. G., C. S., and C. H. J. M. S. S. designed and implemented the process automation module of the self-driving fluidic lab with J. A. B. and A.V. S. S., J. G., and C. S. conducted the partial grid search and autonomous nanocrystal synthesis campaigns. P. J., N. M., and C.S. helped with the precursor chemistry development. P. J., N. M., J. L., A. G., and A. V. helped with the *ex situ* characterization of nanocrystals. M.A. acquired funding and directed the project. S. S., K. M., and M. A. drafted the manuscript. All authors provided feedback on the manuscript.

Conflicts of interest

The authors declare no conflict of interest.

Acknowledgements

M. A. gratefully acknowledges financial support from the National Science Foundation (Awards #2315996 and 2208406) and the University of North Carolina Research Opportunities Initiative (UNC-ROI) program. This work was performed in part at the Analytical Instrumentation Facility (AIF) at North Carolina State University, which is supported by the State of North Carolina and the National Science Foundation (award number ECCS-1542015). The AIF is a member of the North Carolina Research Triangle Nanotechnology Network (RTNN), a site in the National Nanotechnology Coordinated Infrastructure (NNCI).

References

1 K. Abdel-Latif, F. Bateni, S. Crouse and M. Abolhasani, *Matter*, 2020, **3**, 1053–1086.
2 Y. Bai, M. Hao, S. Ding, P. Chen and L. Wang, *Adv. Mater.*, 2022, **34**, 2105958.
3 M. V. Kovalenko, L. Protesescu and M. I. Bodnarchuk, *Science*, 2017, **358**, 745–750.
4 A. F. Gualdrón-Reyes, S. Masi and I. Mora-Seró, *Trends Chem.*, 2021, **3**, 499–511.
5 Y. Zhang, T. D. Siegler, C. J. Thomas, M. K. Abney, T. Shah, A. De Gorostiza, R. M. Greene and B. A. Korgel, *Chem. Mater.*, 2020, **32**, 5410–5423.
6 A. Pan, B. He, X. Fan, Z. Liu, J. J. Urban, A. P. Alivisatos, L. He and Y. Liu, *ACS Nano*, 2016, **10**, 7943–7954.
7 H. Huang, R. Li, S. Jin, Z. Li, P. Huang, J. Hong, S. Du, W. Zheng, X. Chen and D. Chen, *ACS Appl. Mater. Interfaces*, 2021, **13**, 34561–34571.
8 S. Yakunin, L. Protesescu, F. Krieg, M. I. Bodnarchuk, G. Nedelcu, M. Humer, G. De Luca, M. Fiebig, W. Heiss and M. V. Kovalenko, *Nat. Commun.*, 2015, **6**, 8056.
9 P. Ramasamy, D.-H. Lim, B. Kim, S.-H. Lee, M.-S. Lee and J.-S. Lee, *Chem. Commun.*, 2016, **52**, 2067–2070.
10 T. Cai, J. Wang, W. Li, K. Hills-Kimball, H. Yang, Y. Nagaoka, Y. Yuan, R. Zia and O. Chen, *Adv. Sci.*, 2020, **7**, 2001317.
11 T. Wei, K. Lian, J. Tao, H. Zhang, D. Xu, J. Han, C. Fan, Z. Zhang, W. Bi and C. Sun, *ACS Appl. Mater. Interfaces*, 2022, **14**, 44572–44580.
12 V. I. Klimov, T. A. Baker, J. Lim, K. A. Velizhanin and H. McDaniel, *ACS Photonics*, 2016, **3**, 1138–1148.
13 Z. Luo, Q. Li, L. Zhang, X. Wu, L. Tan, C. Zou, Y. Liu and Z. Quan, *Small*, 2020, **16**, 1905226.
14 Y. Li, P. Vashishtha, Z. Zhou, Z. Li, S. B. Shivarudraiah, C. Ma, J. Liu, K. S. Wong, H. Su and J. E. Halpert, *Chem. Mater.*, 2020, **32**, 5515–5524.
15 Y. Lu, S. Fang, G. Li and L. Li, *J. Alloys Compd.*, 2022, **903**, 163924.
16 S. Seth and A. Samanta, *J. Phys. Chem. Lett.*, 2018, **9**, 176–183.
17 C. Zhou, H. Lin, Q. He, L. Xu, M. Worku, M. Chaaban, S. Lee, X. Shi, M.-H. Du and B. Ma, *Mater. Sci. Eng., R*, 2019, **137**, 38–65.
18 H. Lin, C. Zhou, Y. Tian, T. Siegrist and B. Ma, *ACS Energy Lett.*, 2018, **3**, 54–62.
19 M. D. Smith, B. A. Connor and H. I. Karunadasa, *Chem. Rev.*, 2019, **119**, 3104–3139.
20 S. Li, J. Luo, J. Liu and J. Tang, *J. Phys. Chem. Lett.*, 2019, **10**, 1999–2007.
21 Z.-X. Zhang, C. Li, Y. Lu, X.-W. Tong, F.-X. Liang, X.-Y. Zhao, D. Wu, C. Xie and L.-B. Luo, *J. Phys. Chem. Lett.*, 2019, **10**, 5343–5350.
22 F. Cao, X. Xu, D. Yu and H. Zeng, *Nanophotonics*, 2021, **10**, 2221–2247.
23 J. Zhou, K. An, P. He, J. Yang, C. Zhou, Y. Luo, W. Kang, W. Hu, P. Feng, M. Zhou and X. Tang, *Adv. Opt. Mater.*, 2021, **9**, 2002144.
24 N. Zhang, K. Xia, Q. He and J. Pan, *ACS Mater. Lett.*, 2022, **4**, 1233–1254.
25 W. Cui, J. Zhao, L. Wang, P. Lv, X. Li, Z. Yin, C. Yang and A. Tang, *J. Phys. Chem. Lett.*, 2022, **13**, 4856–4863.
26 L. Lian, M. Zheng, W. Zhang, L. Yin, X. Du, P. Zhang, X. Zhang, J. Gao, D. Zhang, L. Gao, G. Niu, H. Song, R. Chen, X. Lan, J. Tang and J. Zhang, *Adv. Sci.*, 2020, **7**, 2000195.
27 J. A. Bennett and M. Abolhasani, *Curr. Opin. Chem. Eng.*, 2022, **36**, 100831.
28 R. W. Epps and M. Abolhasani, *Appl. Phys. Rev.*, 2021, **8**, 041316.
29 A. A. Volk, Z. S. Campbell, M. Y. S. Ibrahim, J. A. Bennett and M. Abolhasani, *Annu. Rev. Chem. Biomol. Eng.*, 2022, **13**, 45–72.
30 K. F. Jensen, *AIChE J.*, 2017, **63**, 858–869.
31 M. Abolhasani, K. A. Brown and G. Editors, *MRS Bull.*, 2023, **48**, 134–141.
32 M. Abolhasani and E. Kumacheva, *Nat. Synth.*, 2023, **2**, 483–492.
33 A. A. Volk, R. W. Epps and M. Abolhasani, *Adv. Mater.*, 2021, **33**, 2004495.
34 R. W. Epps, A. A. Volk, M. Y. S. Ibrahim and M. Abolhasani, *Chem*, 2021, **7**, 2541–2545.
35 S. Sadeghi, F. Bateni, T. Kim, D. Y. Son, J. A. Bennett, N. Orouji, V. S. Punati, C. Stark, T. D. Cerra, R. Awad, F. Delgado-Licona, J. Xu, N. Mukhin, H. Dickerson, K. G. Reyes and M. Abolhasani, *Nanoscale*, 2024, **16**, 580–591.
36 F. Bateni, S. Sadeghi, N. Orouji, J. A. Bennett, V. S. Punati, C. Stark, J. Wang, M. C. Rosko, O. Chen, F. N. Castellano, K. G. Reyes and M. Abolhasani, *Adv. Energy Mater.*, 2024, **14**, 2302303.
37 K. Qu, Y. Lu, P. Ran, K. Wang, N. Zhang, K. Xia, H. Zhang, X. Pi, H. Hu, Y. (Michael) Yang, Q. He, J. Yin and J. Pan, *Adv. Opt. Mater.*, 2023, **11**, 2202883.
38 R. W. Epps, A. A. Volk, K. Abdel-Latif and M. Abolhasani, *React. Chem. Eng.*, 2020, **5**, 1212–1217.
39 Y. Qian, Y. Shi, G. Shi, G. Shi, X. Zhang, L. Yuan, Q. Zhong, Y. Liu, Y. Wang, X. Ling, F. Li, M. Cao, S. Li, Q. Zhang, Z. Liu and W. Ma, *Sol. RRL*, 2021, **5**, 2100090.
40 I. Lignos, S. Stavrakis, G. Nedelcu, L. Protesescu, A. J. deMello and M. V. Kovalenko, *Nano Lett.*, 2016, **16**, 1869–1877.
41 J. Chen, Y. Li, Z. Yin, S. Wang, O. Lin, W. Niu, F. Teng and A. Tang, *J. Mater. Chem. C*, 2023, **11**, 13030–13038.

42 C.-X. Li, S.-B. Cho, D.-H. Kim and I.-K. Park, *Chem. Mater.*, 2022, **34**, 6921–6932.
43 T. Jun, K. Sim, S. Iimura, M. Sasase, H. Kamioka, J. Kim and H. Hosono, *Adv. Mater.*, 2018, **30**, 1804547.
44 K. Chen, A. Bothwell, H. Guthrey, M. B. Hartenstein, J.-I. Polzin, F. Feldmann, W. Nemeth, S. Theingi, M. Page, D. L. Young, P. Stradins and S. Agarwal, *Sol. Energy Mater. Sol. Cells*, 2022, **236**, 111510.
45 P. Jha, N. Mukhin, A. Ghorai, H. Morshedian, R. B. Canty, F. Delgado-Licona, E. E. Brown, A. J. Pyrch, F. N. Castellano and M. Abolhasani, *Adv. Mater.*, 2025, **37**(16), 2419668.